Shock-compressed $MgSiO_3$ glass, enstatite, olivine, and quartz: Optical emission, temperatures, and melting

Sheng-Nian Luo

Plasma Physics (P-24) and Earth and Environmental Sciences (EES-11), Los Alamos National Laboratory, Los Alamos, New Mexico, USA

Lindhurst Laboratory of Experimental Geophysics, Seismological Laboratory, California Institute of Technology, Pasadena, California, USA

Joseph A. Akins and Thomas J. Ahrens

Lindhurst Laboratory of Experimental Geophysics, Seismological Laboratory, California Institute of Technology, Pasadena, California, USA

Paul D. Asimow

Division of Geological and Planetary Sciences, California Institute of Technology, Pasadena, California, USA

Received 20 October 2003; revised 3 March 2004; accepted 10 March 2004; published 11 May 2004.

[1] Optical emission of $MgSiO_3$ glass, enstatite, olivine, and quartz under shock wave compression was investigated with optical pyrometry at discrete wavelengths ranging from visible to near infrared. We develop a new analysis of optical emission that does not require a gray body assumption. Instead, at each wavelength, the optical linear absorption coefficients (a) and blackbody spectral radiances ($L_{\lambda b}$) of shocked and unshocked materials were obtained by nonlinear fitting to the time-resolved radiance from the target assembly. The absorption spectra of unshocked samples corresponding to the measured values of a reproduce those from independent static optical spectroscopic measurements. The measured values of a (ranging from 7 to 56 mm^{-1}) for shocked samples indicate that shock-induced high-pressure phases (including melt) can be regarded essentially as black bodies in the optical range investigated, although starting phases such as enstatite and olivine have band-like spectra at ambient conditions. The effect of emission from the air gap at the driver sample interface on the recorded radiance can be resolved, but a and $L_{\lambda b}$ cannot be separated for this component of the signal. The shock velocity-particle velocity relationships of these silicates derived from radiance history are in accord with previous investigations using independent techniques. Given the limited amount of shock wave data, possible high-pressure melting curves of Mg-perovskite and its assemblage with periclase are deduced; their melting temperatures near the core-mantle boundary (CMB) being 6000 ± 500 K and 4000 ± 300 K, respectively. It is proposed that Mg-perovskite melts with density increase at the CMB pressure. *INDEX TERMS:* 3924 Mineral Physics: High-pressure behavior; 3939 Mineral Physics: Physical thermodynamics; 3944 Mineral Physics: Shock wave experiments; *KEYWORDS:* shock temperature, melting, equation of state, pyrometry, silicates, perovskite

Citation: Luo, S.-N., J. A. Akins, T. J. Ahrens, and P. D. Asimow (2004), Shock-compressed $MgSiO_3$ glass, enstatite, olivine, and quartz: Optical emission, temperatures, and melting, *J. Geophys. Res.*, *109*, B05205, doi:10.1029/2003JB002860.

1. Introduction

[2] Progress in the application of modern seismic techniques ranging from travel time tomography to waveform modeling continues to yield improved knowledge of the three-dimensional structure of longitudinal and shear wave velocities and density of the Earth's deep interior [*Grand et al.*, 1997; *Ni et al.*, 2002]. Converting such observations into constraints on the chemical, mineralogical, and thermal state of the mantle requires detailed understanding of the equations of state (EOS) and phase transitions (both solid-solid and melting) of candidate minerals. Of particular interest are the low- and ultra-low velocity zones (ULVZ) found in the lowermost mantle near the core-mantle boundary (CMB) [*Garnero and Helmberger*, 1995]. The velocity reductions associated with these anomalies are so extreme that partial melting appears to be the only interpretation allowed by mineral physics. Understanding the consequences of such melting demands detailed knowledge of phase relations and physical properties for the major (and, eventually, minor components) of the lower mantle, presumably silicates and oxides such as $(Mg,Fe)_2SiO_4$, $(Mg,Fe)SiO_3$,

0148-0227/04/2003JB002860$09.00

(Mg,Fe)O and perhaps SiO_2. Static high-pressure experiments in the multianvil apparatus and diamond-anvil cell (DAC) have provided some constraints on the melting behavior of such minerals [*Zerr and Boehler*, 1993; *Shen and Lazor*, 1995; *Heinz and Jeanloz*, 1987; *Kato and Kumazawa*, 1985]. Limitations on the pressure and temperature capability of these systems, however, mean that melting of some of these components has not been characterized above 100 GPa; there are also major discrepancies among the measured or extrapolated melting curves derived from DAC observations for some components. First-principles and molecular dynamics simulations of such complicated silicate systems remain challenging, and at present must still be validated against accurate experimental results. In dynamic techniques such as planar shock wave loading, samples are compressed and heated simultaneously, thus melting points above 100 GPa can in principle be measured, although studies with such techniques suffer from scanty data and possible kinetic behavior such as superheating [*Boness and Brown*, 1993; *Luo and Ahrens*, 2003; *Luo et al.*, 2003a; *Luo and Ahrens*, 2004]. Currently, shock wave loading serves as a major practical approach to resolving melting at pressures directly relevant to the lowermost mantle. In this work, we intend to probe the melting behavior of $MgSiO_3$ perovskite (hereafter, Pv) and the analogue lower mantle assemblage Pv plus periclase.

[3] No shock temperature data are available for Pv. Although we have not used Pv as an ambient pressure starting material in this study, we expect that Pv forms upon shock wave loading of $MgSiO_3$ glass or of crystalline enstatite for shock pressure greater than about 60 GPa [*Brown et al.*, 1987b]. Previously, the long-range order of shocked Si and Ga has been observed [*Swift et al.*, 2001; *Luo et al.*, 2004] with in situ time-resolved X-ray diffraction techniques. We take this as an indication that the crystalline phases may also form during shock wave loading of silicates. As $MgSiO_3$ glass is less dense than enstatite at ambient conditions, glass starting material shocks to higher temperature states (at a given compressed density) than enstatite, and so shock-synthesized perovskite melts at lower pressure on the principal Hugoniot of glass than on that of enstatite. Both starting materials are investigated in this work in order to obtain constraints on the melting of Pv at different pressures.

[4] The shock wave equations of state [*Jackson and Ahrens*, 1979; *Brown et al.*, 1987b] and high-pressure sound speed [*Brown et al.*, 1987a] have previously been measured for forsterite and olivine. Shock melting of forsterite and olivine has been investigated using optical pyrometry to infer shock temperatures [*Lyzenga and Ahrens*, 1980; *Holland and Ahrens*, 1997]. At similar pressures, the temperatures inferred by *Holland and Ahrens* [1997] are significantly higher than those by *Lyzenga and Ahrens* [1980], possibly due to the low emissivity obtained in the former study, which also found unexplained dramatic differences in emissivities at slightly different pressures for the same phases (e.g., $\epsilon \sim 0.03$ and 0.3 at 184 and 192 GPa, respectively). We have reanalyzed the olivine data of these authors accounting, for the first time, for optical linear absorption of the unshocked sample through which the shock front radiation is observed.

[5] Previous studies utilizing optical pyrometry assumed gray body radiation and used whole-spectrum fitting to obtain emissivity and temperature. However, the emissivity (and blackbody spectral radiance) can be determined separately and independently at each individual wavelength from time-resolved radiation recordings [*Boslough*, 1985]. This approach is less susceptible to scatter of measurements among different wavelengths and is able to deal with nongray body spectral features. This technique is of particular advantage for unshocked materials with band-like absorption spectra such as Fe-bearing olivine and orthopyroxene that complicate the radiation history of shocked samples. Besides optical properties and temperature, the radiation history contains a recording of shock front velocity and hence can be inverted for equation of state, which is usually measured with different diagnostic technology. As quartz is well-studied with various techniques including shock temperature measurement, it is included in present study as a technical reference. We begin by reviewing the methodology of optical pyrometry followed by experiments and data analysis sections. We end with a discussion of the geophysical implications of these results.

2. Methodology

[6] Optical pyrometry is the use of optical emission measurements to determine the temperature and optical properties of shock-compressed materials [*Kormer*, 1965; *Boslough and Ahrens*, 1989]. We review here the justification for application of Planck's formula, typical experimental designs and methods for data reduction. We assume that the observed optical signal is thermal radiation and that the electron temperature equilibrates to that of the lattice on the timescales of shock wave loading.

[7] Photons are bosons obeying Bose-Einstein statistics (e.g., *Fowles* [1989]). At equilibrium, the mean occupation number of photons at certain state centered at frequency ν is $\langle n \rangle = 1/e^{h\nu/kT} - 1$ where T is temperature, h Planck's constant and k the Boltzmann constant. The density of number of states per unit frequency interval is $g_\nu = 8\pi\nu^2/c^3$ where c is the speed of light. Thus the energy density (e) per unit frequency interval is

$$e_\nu \equiv \mathrm{d}e/\mathrm{d}\nu = \frac{8\pi h\nu^3}{c^3}\frac{1}{e^{h\nu/kT}-1}, \tag{1}$$

i.e., Planck's formula for blackbody radiation. The energy flux per unit frequency interval is $J_\nu = ce_\nu/4$, and can be converted to its counterpart in wavelength (λ) with $\nu = c/\lambda$ and $\mathrm{d}\nu = -(c/\lambda^2)\mathrm{d}\lambda$. The spectral radiance $L_{\lambda b} = J_\lambda/\pi$ for a blackbody

$$L_{\lambda b} = \frac{c_1}{\lambda^5}\frac{1}{e^{c_2/\lambda T}-1} \tag{2}$$

where $c_1 = 2hc^2 \approx 1.191 \times 10^{-16}$ Wm^2 sr^{-1}, and $c_2 = hc/k \approx 1.439 \times 10^{-2}$ mK. $L_{\lambda b}$ is essentially the energy flux per unit wavelength interval per unit solid angle (Wm^{-3} sr^{-1}). As a light source is not necessarily a blackbody, the spectral radiance is written in a more general form as $L_\lambda = \epsilon(\lambda, T)L_{\lambda b}$ where ϵ is emissivity and assumed to depend on λ and T only.

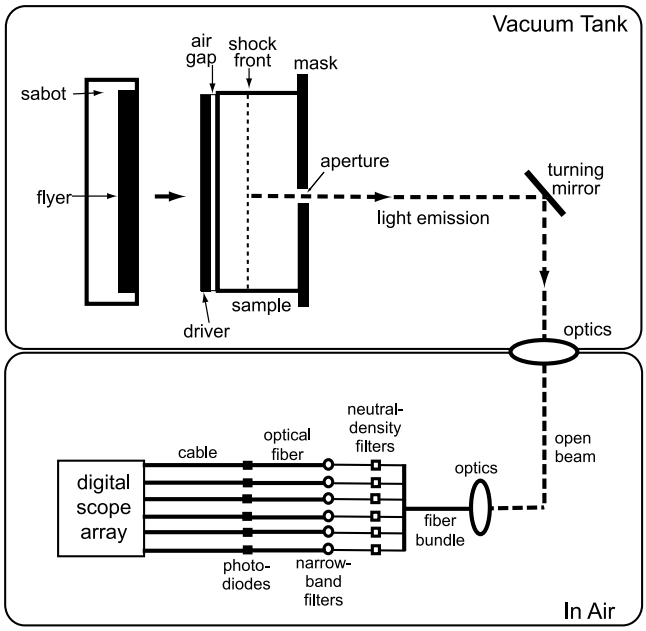

Figure 1. Schematic diagram of a six-channel optical pyrometer for shock temperature measurement. Air gap may be present at driver-sample interface. Light emitted from behind shock front passes through aperture of mask. Expendable turning mirror and optics relay light to six neutral-density and narrow-band color filters. Adjustable neutral-density filters on each channel allow the dynamic range of the system to be optimized for the expected radiance spectrum in each experiment. An array of photodiodes [*Holland*, 1997] convert light from each color filter into electrical signals recorded as time-resolved voltages by digital oscilloscopes.

[8] To determine the temperature of a radiating sample upon shock wave compression, we need to know L_λ and $\epsilon(\lambda, T)$. In practice, a multichannel pyrometer (Figure 1) is utilized to measure L_λ at discrete wavelengths with narrow-band-pass optical filters (~9 nm half-height bandwidth). Calibration is required to obtain the absolute values of L_λ with a spectral radiance or irradiance source. The latter is adopted in this work. A quartz-halogen tungsten-filament lamp with spectral irradiance I_λ (Figure 2; Note that the unit need be converted to $\mathrm{Wm^{-1}\,sr^{-1}}$) is placed in the position of the target for calibration before mounting target for shock wave loading. The optical path is kept the same for calibration and experiment. Photodetectors with ~nanosecond response time convert photon signals into voltage signals recorded by digital oscilloscopes normally at 10^9 samples/s. The voltage for the calibration (V_{lamp}, Figure 2 insert),

$$V_{\mathrm{lamp}} \propto \int_\lambda \int_\Omega I_\lambda(\lambda, \Omega) H(\lambda) \mathrm{d}\lambda \mathrm{d}\Omega \tag{3}$$

where Ω is solid angle, and $H(\lambda)$ is the response function of the optical path including narrow-band filter centered at a certain wavelength λ_0. Similarly, for shock-loaded sample,

$$V_{\mathrm{sample}} \propto \int_\lambda \int_\Omega \int_{S_{\mathrm{mask}}} L_\lambda(\lambda, T, \Omega) H(\lambda) \mathrm{d}\lambda \mathrm{d}\Omega \mathrm{d}S \tag{4}$$

where S denotes area, and S_{mask} is the area of the aperture in the mask. Suppose that radiation is isotropic and the response of the narrow-band filter $\propto \delta(\lambda - \lambda_0)$, then

$$L_\lambda = \frac{V_{\mathrm{sample}}}{V_{\mathrm{lamp}}} \frac{I_\lambda}{S_{\mathrm{mask}}} \tag{5}$$

where a linear response of the photodetector to photon flux (before saturation) is assumed.

[9] A general target assembly during shock is composed of an air gap at the driver-sample interface, some already shocked sample and some not-yet-shocked sample (denoted with subscripts air, s, and u, respectively; Figure 1). The observed L_λ depends on the temperature and linear absorption coefficients (a) of all three of these elements of the system as well as the reflectivity (R) of the interfaces. Assuming local thermodynamic equilibrium, emissivity (ϵ) of a non-reflecting layer of thickness d is equal to absorbance, i.e., $\epsilon = 1 - e^{-ad}$. Thus the observed spectral radiance

$$\begin{aligned} L_\lambda = {} & L_{\lambda b,\mathrm{air}}(1-R_1)(1-R_2)(1-R_3)\epsilon_{\mathrm{air}} e^{-a_s d_s} e^{-a_u d_u} \\ & + L_{\lambda b,s}(1-R_2)(1-R_3)\left(1-e^{-a_s d_s}\right)e^{-a_u d_u} \\ & + L_{\lambda b,u}(1-R_3)\left(1-e^{-a_u d_u}\right) \end{aligned} \tag{6}$$

consists of contributions from the air gap, shocked and unshocked sample where $L_{\lambda b,s}$ is the quantity of main

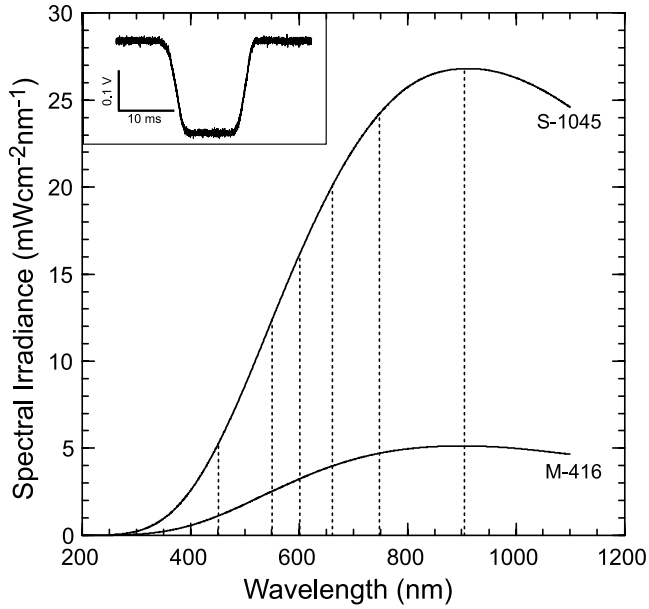

Figure 2. Spectral irradiance I_λ of quartz-halogen tungsten coiled filament lamps S-1045 (operated at 1000 W and 8 A) and M-416 (200 W and 6.5 A), interpolated with cubic spline from calibrations by Optronic Laboratories. Here I_λ is defined as the power per unit wavelength intercepted by a 1 $\mathrm{cm^2}$ detector, 50 cm from center of filament. Note that to apply values of I_λ in equations (4) and (5), one needs to convert units to power per unit wavelength per unit solid angle. Vertical dotted lines denote the wavelengths of narrow-band filters adopted in the current pyrometer. The insert shows a typical calibration record (voltage versus time) at λ = 551.0 nm for S-1045.

Table 1. Electron Microprobe Analysis of Enstatite Glass and Crystal (Weight Percents of Oxides)

Material	SiO_2	TiO_2	Al_2O_3	Cr_2O_3	FeO	MnO	MgO	NiO	CaO	Na_2O	K_2O	Sum
Crystal	59.825	0.028	1.530	0.006	0.336	0.005	39.916	0.008	0.126	0.007	0.002	100.820
Glass	62.247	0.000	0.050	0.000	0.221	0.024	38.026	0.000	0.174	0.000	0.017	100.760

interest. If experiments are conducted without significant sample preheating, the 3rd term on the right-hand side of equation (6) can be neglected. Interface reflectivity $R_i = (\frac{n_i-1}{n_i+1})^2$ where n_i (i = 1, 2 and 3, denoting air – sample, shocked – unshocked sample and sample – free surface interfaces respectively) is the relative index of refraction across the interface. As n_i is wavelength-dependent and its values are not available (at high pressures), we assume $R \sim 0$ as in previous studies [*Lyzenga et al.*, 1983]. For a shock state with shock velocity U_s and particle velocity u_p, $d_s = (U_s - u_p)t$ and $d_u = d_0 - U_s t$ where d_0 is the initial sample thickness and t the time after the shock front enters the sample.

[10] Previous studies mostly assumed gray (or black) body radiation, such that at each time during the experiment single values of emissivity and temperature are obtained simultaneously from fitting to $L_\lambda = \epsilon(T)L_{\lambda b}$. The gray body assumption is difficult to justify a priori. Instead we show in this paper that the time-evolution of the recorded radiation over the course of the shock transit through the experiment in fact contains information on temperature and emissivity. This allows a (and hence ϵ) and $L_{\lambda b}$ to be obtained from non-linear fitting to equation (6). The values of $L_{\lambda b}$ at different wavelengths then allow temperature to be determined by fitting $L_{\lambda b}(\lambda)$ to equation (2). This results in independent values of ϵ at each wavelength, independent of calibration and requiring no gray body assumption. Although the principle has been described before [*Boslough*, 1985], this method has not previously been applied rigorously to real data.

3. Experiments

[11] We carried out shock temperature measurements on synthetic x-cut single-crystal α-quartz (Adolf Meller Co.), synthetic $MgSiO_3$ glass and natural enstatite (Tables 1 and 2). Our primary interest here is in the $MgSiO_3$ system, but given the significant amount of shock wave data available for quartz [*Lyzenga et al.*, 1983], we conducted a diagnostic quartz shot to test the pyrometer and the new data reduction technique and to provide a reference for data analysis in unknown experiments. $MgSiO_3$ glass is synthesized by melting an equimolar mixture of Johnson-Matthey high-purity MgO and SiO_2 powders at 1650°C and carefully regulating the water-quench procedure to suppress both cracking and forsterite crystallization. The natural enstatite samples are cut from gem quality single crystals from Sri Lanka. Electron microprobe analysis on both glass and enstatite revealed chemical compositions of essentially $MgSiO_3$ (Table 1). Both $MgSiO_3$ glass and enstatite are colorless and nearly transparent to visible light. We measured their absorption spectra in the range of 300–1100 nm (Figure 3). The absorbance of $MgSiO_3$ glass decreases with λ but cannot be described by λ^{-4} as in Rayleigh scattering [*Jackson*, 1975]. Enstatite demonstrates three absorption peaks with a pronounced one near 900 nm as expected [*Burns*, 1993]. Note that the values for absorbance vary with optical setup and sample thickness, and are meaningful only in a relative sense.

[12] Samples are sectioned into disks and polished to appropriate thickness to minimize edge effects. Both sides are of submicron-micron smoothness, and one side is coated with a thin Al layer by evaporation. The coated side of the sample is then glued in tight contact with a finely polished metal driver plate. An air gap of varying thickness forms at the driver-sample interface. The Al coating is intended to block radiation from the shocked air gap into the sample, but its effectiveness strongly depends on the strength of coating. The air gap can be minimized by improving further the polish on the contacting surfaces of sample and driver plate. (As shown later, the effect of the air gap can be resolved in our experiments, possibly yielding extra information on the shock behavior of air.)

[13] The calibration lamp (S-1045 for quartz, $MgSiO_3$ glass and enstatite shots) is placed at the sample position prior to installing target. A typical calibration voltage trace is shown in Figure 2 (insert) from which V_{lamp} is determined as offset of the plateau from the baseline. Then the target assembly is installed without altering the optical path and the chamber is closed and evacuated for shooting on the two-stage light-gas gun at Caltech. Each pyrometer channel output is recorded by 2–4 oscilloscope channels. The voltage signal (V_{sample}) is then converted to apparent spectral radiance L_λ using the calibration voltage V_{lamp}, the lamp spectral irradiance (I_λ, Figure 2), the mask area and equation (5). Figure 4 displays representative time-resolved spectral radiances of shocked $MgSiO_3$ glass (shot 335) recorded by the six-channel pyrometer.

[14] As we will reanalyze the previous data on olivine [*Holland and Ahrens*, 1997], we briefly discuss the exper-

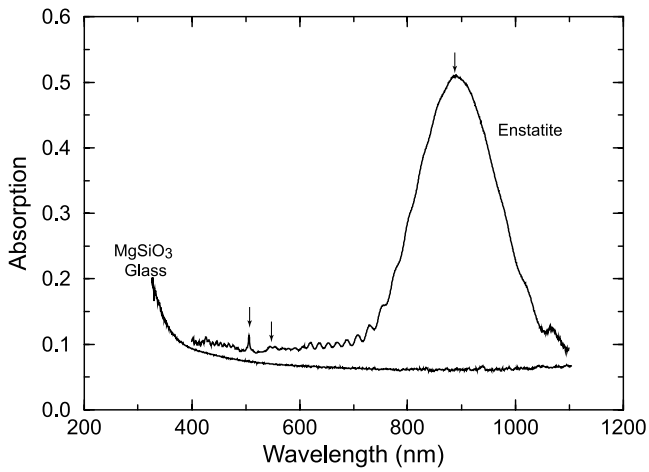

Figure 3. Representative optical absorption spectra of synthetic $MgSiO_3$ glass and natural enstatite crystal. Arrows indicate absorption peaks of enstatite as by *Burns* [1993].

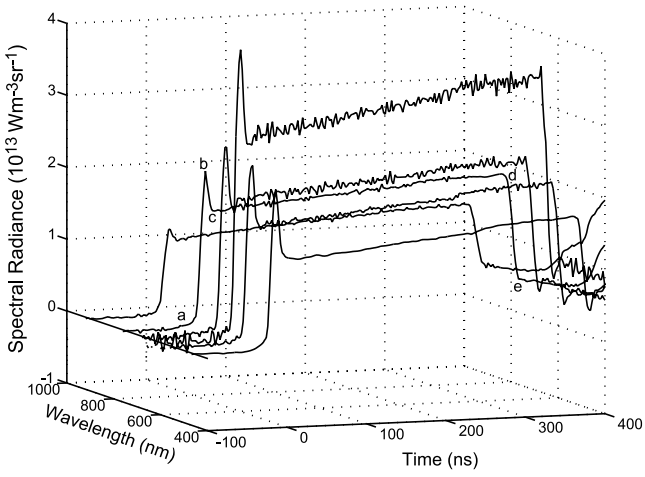

Figure 4. Representative time-resolved radiance profiles recorded by the six-channel pyrometer ($MgSiO_3$ glass, shot 335). Times marked $a - e$ correspond to key events discussed in text upon loading and unloading.

iment. Samples were San Carlos and Burma peridot with compositions close to $(Mg_{0.9}Fe_{0.1})_2SiO_4$. Optical spectroscopy of starting materials revealed a slight decrease of absorbance with wavelength in the 450–560 nm range, a shallow increase at 560–700 nm and a significant increase beyond 700 nm [*Holland*, 1997]. The experiment was similar to those for quartz, $MgSiO_3$ glass and enstatite except that the calibration lamp was M-416 (Figure 2). Previous experiments on forsterite [*Lyzenga and Ahrens*, 1980] adopted similar technique.

4. Data Analysis

[15] Typical spectral radiance histories of quartz, olivine, $MgSiO_3$ glass and enstatite are shown in Figures 4 and 5. As we will see, some of the distinctive appearances of these spectra result from the differing absorbance properties of the unshocked sample materials; some features result from imperfect emission by the shocked sample early in the experiment when the shocked layer is very thin; other features result from differences in the intensity of the air

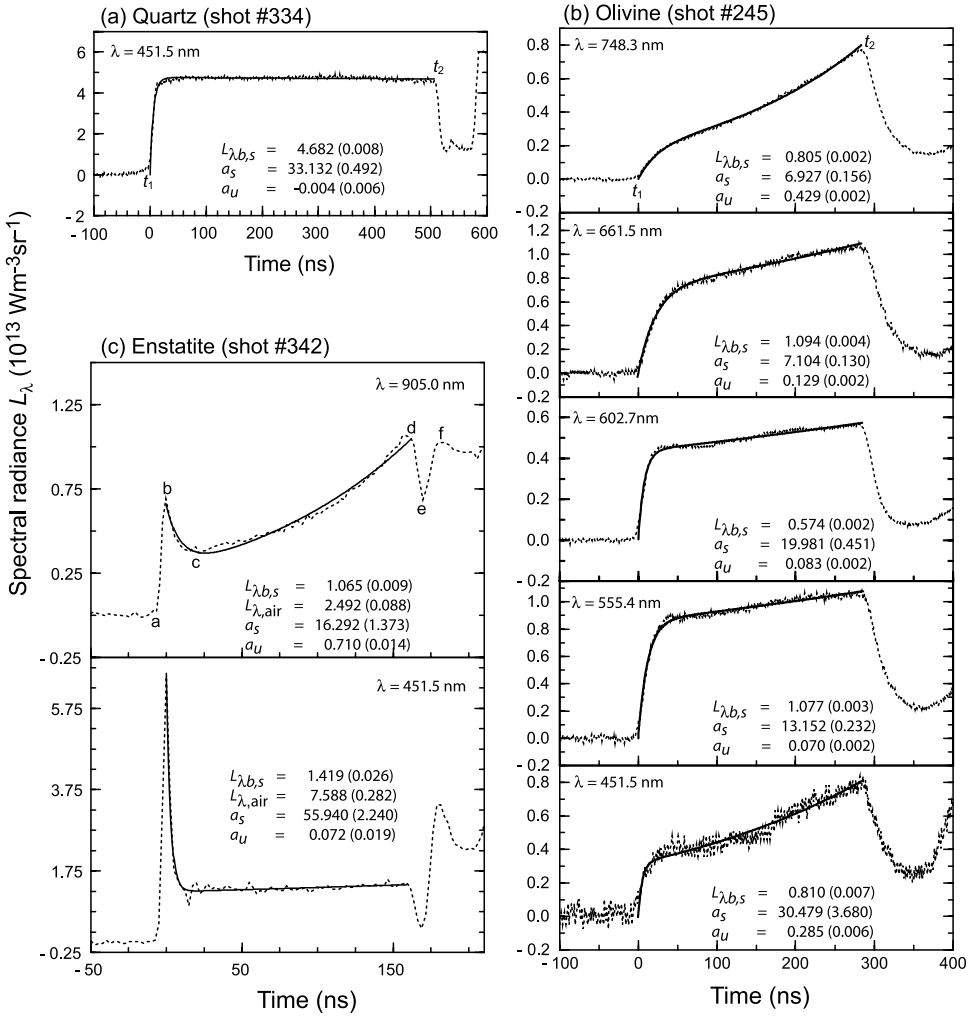

Figure 5. Time-resolved spectral radiance from (a) shocked quartz (shot 334), (b) olivine (245) and (c) enstatite (342). Dotted curves denote shock recordings, and solid curves are models fits using equation (6). The fitted parameters shown on each panel. $L_{\lambda b}$ is given in units of 10^{13} Wm^{-3} sr^{-1}; a_s and a_u are in mm^{-1}. Values in parentheses indicate uncertainties in the fitting. In (c), points $a - f$ denote significant events in loading and unloading history (see text) and $L_{\lambda,\mathrm{air}} = \epsilon_{\mathrm{air}} L_{\lambda b,\mathrm{air}}$.

Table 2. Shock Wave Experiments Parameters[a]

Shot #	Starting Material	d (mm)	ϕ (mm)	ρ_0 (g/cm^3)	u_{fp} (km/s)	P_H (GPa)	U_s (km/s)	u_p (km/s)	ρ (g/cm^3)	T_H (K)
245	Olivine	3.38	6.35	3.36	6.82	188(6)	11.46(16)	4.89(15)	5.86(15)	4810(70)
334	Quartz	4.78	2.11	2.65	5.64	106(1)	9.23(7)	4.36(4)	5.02(5)	6680(420)
335	En. Glass	3.85	2.02	2.75	5.67	117(3)	9.85(10)	4.30(8)	4.88(8)	5580(130)
336	En. Glass	2.54	2.10	2.73	5.88	121(4)	9.92(16)	4.47(13)	4.96(13)	5940(560)
340	En. Crystal	1.86	2.02	3.19	5.85	142(7)	10.47(24)	4.26(18)	5.38(17)	4130(50)
341	En. Crystal	1.88	1.98	3.19	6.38	165(8)	11.17(27)	4.62(20)	5.44(19)	4900(140)
342	En. Crystal	1.95	1.98	3.23	6.79	183(9)	11.59(28)	4.89(21)	5.59(20)	5450(100)

[a]Flyer and driver are Ta plates. Values in parentheses denote uncertainties. Errors in d, ρ_0 and u_{fp} are negligible. ϕ is the diameter of the aperture in the mask.

gap flash due to variations in driver and sample polishing and Al coating. To illustrate the general physical process, the interpretation of the various parts of these records is shown using lettered time markers as in Figures 4 and 5c. First, the shock reaches the rear surface of the opaque driver at point *a*. Some records show a sharp rise in intensity *ab* as the shock reverberates in the air gap at the driver-sample interface. The air is compressed to peak pressure and its temperature rises in less than 10 ns to a level significantly higher than the sample. Once the shock enters the sample, the transmission of the air radiance decreases rapidly (*bc* segment, Figures 4 and 5c) mostly due to the screening effect of an increasing thickness of shocked sample. On the other hand, particularly in cases where the unshocked material is significantly absorbing, radiance turns around and increases again during *cd*. As the shock propagates through the sample, this interval reflects the increasing thickness (and thus emissivity) of the shocked sample and the decreasing thickness and hence absorption of the unshocked sample. The shock reaches the rear surface of the sample at time *d*; segment *de* shows the temperature and radiance decrease upon release. The reason for the later rise of radiance (*ef*) is not clear; possibly this is due to reshock on the metal mask. The exact shape certainly depends on the optical properties at shocked, unshocked and release states. The air gap is absent in quartz and olivine shots, thus the recordings are simpler. More quantitative analysis can be obtained from equation (6) using the following procedure.

[16] Fitting the observed spectral radiance to equation (6) yields $L_{\lambda b}$, a_s and a_u (and possibly the product $\epsilon_{\text{air}} L_{\lambda b,\text{air}}$ as well) at each wavelength. Emissivity for shocked and unshocked sample can thus be calculated for various thicknesses with $\epsilon = 1 - e^{-ad}$. To obtain temperature, we fit $L_{\lambda b}$ at various wavelengths to equation (2). Note that this neither assumes a gray body spectrum nor need it imply that the material is a blackbody – emissivity is separated from spectral radiance and the fitting of $L_{\lambda b}$'s to equation (2) represents the true temperature.

[17] Besides temperature and optical properties (linear absorption coefficients), the shock wave velocity U_s can also be deduced from the spectral radiance history as $U_s = d_0/\Delta t$ where $\Delta t = t_2 - t_1$ is shock travel time across a distance d_0 (Figures 5a and 5b where the air gap is absent). On records showing a flash from the air gap t_1 is obscured and times *b* and *d* are chosen as t_1 and t_2, respectively (Figure 5c). The flyer plate velocity (u_{fp}) is obtained from flash X-ray radiography. Without assuming an equation of state (e.g., $U_s - u_p$ relation) of the sample material, the pressure P_H, density ρ and u_p at shock state can be obtained from the impedance match method (jump conditions)

$$\begin{aligned} \rho_{0A} U_{sA} u_p &= \rho_{0B}\left[C_{0B} + s_B\left(u_{fp} - u_p\right)\right]\left(u_{fp} - u_p\right) \\ P_H &= \rho_{0A} U_{sA} u_p \\ \rho_A &= \rho_{0A} U_{sA} / \left(U_{sA} - u_p\right) \end{aligned} \tag{7}$$

where subscript 0 refers to initial condition, *A* refers to the sample and *B* denotes the driver (or, equivalently, the flyer as both driver and flyer are Ta plates). Parameters C_{0B}, s_B and ρ_{0B} are known for Ta standard [*Mitchell and Nellis*, 1981]. Results are summarized in Table 2.

4.1. Quartz

[18] Complete spectral radiance signals were recorded at λ = 451.5, 602.7 and 748.3 nm (the other three channels were off scale) during this diagnostic shot (334). There is no air radiance peak on these records, so we fit the radiance history at each of the three recorded wavelengths to

$$L_\lambda = L_{\lambda b,s}\left[1 - e^{-a_s\left(U_s - u_p\right)t}\right] e^{-a_u\left(d_0 - U_s t\right)} \tag{8}$$

with $L_{\lambda b,s}$, a_s and a_u being unknown parameters. The fitted values of a_s and a_u indicate that shock-synthesized high-pressure phase (stishovite-like) is essentially black (e.g., at $d > 0.2$ mm) and the unshocked pure quartz is totally transparent at these three wavelengths as expected (Figure 5a). Given $L_{\lambda b,s}$ at different wavelengths, we obtain T_H = 6680 ± 420 K from fitting to equation (2). The clear onset and exit times of shock transit through the sample on this record yield good values for U_s, P_H and u_p as well (Table 2). Our (U_s, u_p) values at P_H = 106 GPa agree with R. G. McQueen's $U_s - u_p$ relationship [*Lyzenga et al.*, 1983]: U_s(km/s) = 1.241(0.160) + 1.850(0.045) u_p.

[19] *Lyzenga and Ahrens* [1980] obtained $\epsilon \sim 1$ and 5820 ± 150 K at 106.5 GPa assuming gray body radiation. Their whole-spectrum fitting indicates the high-pressure phase is blackbody like, consistent with our values of a_s from non-linear fitting to the radiation history obtained in our separate shot. If the unshocked material is totally transparent and the shock-synthesized phase black as appears to be the case for quartz, the two methods of fitting ought to yield the same result. Our current measurement of T_H = 6680 ± 420 K matches a shock temperature calculation (T_H = 6650 K at 106 GPa) [*Luo et al.*, 2003b] that used an independent measurement of the high-pressure Grüneisen parameter of stishovite [*Luo et al.*, 2002b]. The new

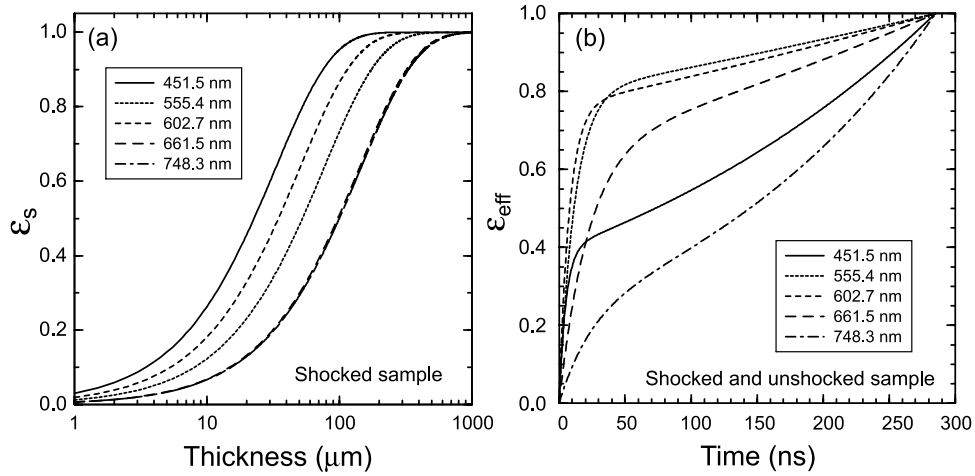

Figure 6. (a) Emissivity (ϵ_s) of high-pressure phases from shocked olivine (shot 245) as a function of thickness of shocked material. (b) Evolution of the effective emissivity ($\epsilon_{\rm eff} = [1 - e^{-a_s(U_s-u_p)t}]e^{-a_u(d_0-U_st)}$) of the whole sample assemblage for last 285 ns in shot 245.

measurement, however, is slightly higher than the 5820 ± 150 K obtained by *Lyzenga and Ahrens* [1980]. The discrepancy could be due to the fact that only three channels were recorded in our shot 340 or perhaps to calibration difference for these two shots. We do not have enough data to analyze the difference in detail, but the agreement with calculated shock temperature and known equation of state values provide confidence that our methods for determining emissivity and travel time are valid.

4.2. Olivine $(Mg,Fe)_2SiO_4$

[20] Shock temperature experiments on $(Mg_{0.9}, Fe_{0.1})_2SiO_4$ olivine (denoted as Fo_{90}) [*Holland and Ahrens*, 1997] and Mg_2SiO_4 forsterite (Fo_{100}) [*Lyzenga and Ahrens*, 1980] were previously conducted. However, *Holland and Ahrens* [1997] used the conventional gray body method of determining ϵ, which as we have emphasized is sensitive to calibration errors and can be confounded by spectral features of unshocked and shocked samples. Here we apply our calibration-independent fitting technique for a_s and a_u to reanalyze data from shot 245 on olivine (Figure 5b) [*Holland*, 1997]; this is the only shock-temperature recording of a Fo_{90} experiment that yielded data of sufficient quality for the present analysis technique. Time-resolved radiance signals were obtained at five wavelengths (Figure 5b). These recordings did not give flat-topped spectral radiance signals, indicating that absorption by unshocked material is significant and that an arbitrary choice of time window for gray body fitting could yield inaccurate results. Like the quartz data presented above, the initial flash from air radiance is absent. Thus we fit the observed spectral radiance to equation (8) (Figure 5b). The fitted $a_u(\lambda)$ agrees with the measured absorption spectrum of the unshocked olivine [*Holland*, 1997]. We obtain P_H = 188 GPa and U_s = 11.46 km/s (Table 2), which agree well with the known Hugoniot EOS of olivine, U_s(km/s) = 6.56(0.33) + 1.01(0.08) u_p [*Brown et al.*, 1987b], at the value of u_p = 4.89 km/s given by the impedance match.

[21] However, for shock temperature, fitting our values of $L_{\lambda s,b}$ to equation (2) results in T_H = 4810 ± 70 K, which is significantly lower than the previous result of 6092 ± 310 K [*Holland and Ahrens*, 1997], but similar to the forsterite result of *Lyzenga and Ahrens* [1980] at slightly lower pressures. The relationship of our result to these previous gray body fitting studies can be understood by exploring the behavior of emissivity of the shocked sample (ϵ_s) and the effective emissivity ($\epsilon_{\rm eff}$) observed at the free surface (Figure 6). ϵ_s increases with thickness: $\epsilon_s = 1 - e^{-a_s d_s}$. As shown in Figure 6a, $\epsilon \sim 1$ at $d_s > 1$ mm (i.e., at $\gtrsim$150 ns shock travel time) for these five wavelengths. This indicates that the shocked olivine is essentially blackbody at $d_s >$ 1 mm which is in contrast to ϵ = 0.23 reported by *Holland and Ahrens* [1997]. Corrections are not made for other olivine shots due to the poor quality of recordings, but we expect that the reported values of T_H should have been much lower.

[22] If the observed radiance resulting from emission in the shocked sample and absorption in the unshocked portion of the sample were to be interpreted as radiation from a single gray body, the result would be characterized by an effective emissivity $\epsilon_{\rm eff} = [1 - e^{-a_s(U_s-u_p)t}]e^{-a_u(d_0-U_st)}$. For gray body fitting to the net radiation emerging from the experiment to be appropriate, it is necessary that each channel give the same value of $\epsilon_{\rm eff}$ throughout the analyzed time window. As seen from Figure 6b, the effective radiance calculated with our fitted values of a_s, a_u and other parameters is not gray body until the very end of the record, when the shock exits at the free surface and hence absorption by the unshocked material vanishes. Thus it is not appropriate to use the last 100-ns record for gray body fitting [*Holland and Ahrens*, 1997] – the observed radiance in this window is band-like due to the absorption spectrum of unshocked olivine.

[23] We expect that the $\epsilon \sim 1$ given by our analysis of shot 245 is in fact typical for the high-pressure assemblage of either shocked Fo_{90} or Fo_{100}, despite the emissivities in the range of 0.53–0.66 obtained by *Lyzenga and Ahrens* [1980] using gray body fitting. The published oscilloscope traces shown by *Lyzenga* [1980] indicate plateau-like radiation histories in the three shots between 150–175 GPa similar to that for quartz (Figure 5a), implying that the shocked sample is blackbody like and the unshocked

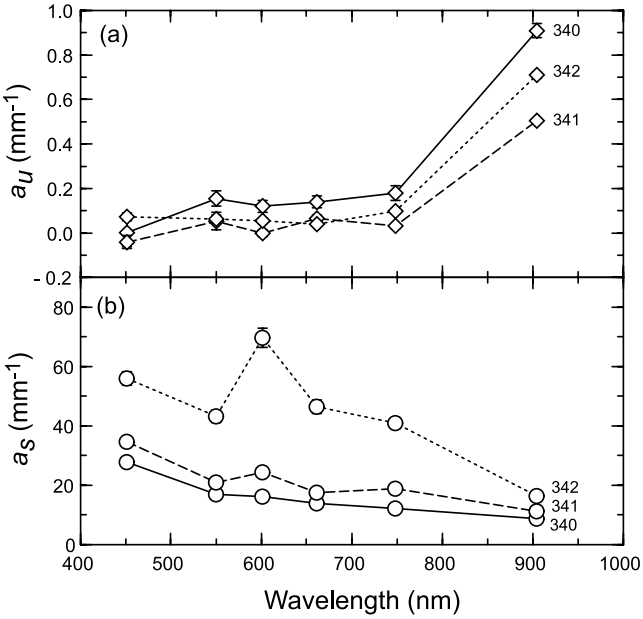

Figure 7. Optical linear absorption coefficients: (a) shocked (a_s) and (b) unshocked (a_u) enstatite (shots 340–342). Note pronounced absorption peak for a_u at 905 nm agrees with static optical spectroscopy of starting materials (Figure 3), and that shock-synthesized perovskite (once thickness exceeds ~0.1 mm) behaves as a blackbody in this wavelength range.

sample is transparent. As the gray body assumption itself is valid (we regard blackbody as a special case of gray body), we expect the two-parameter fitting should yield emissivity close to 1, to be consistent with the radiation history. However, with a small number of channels, scatter in the data, and possible systematic errors, gray body fitting can easily yield unphysical or inaccurate emissivities due to the trade-off between the two parameters. The point here is that even in cases where the gray body assumption is valid, the numerical fitting does not necessarily yield real emissivity and temperature (see the example in the $MgSiO_3$ section below). *Lyzenga* [1980] showed a record for forsterite shocked to 140 GPa, in which continuously decaying radiation without any plateau was interpreted as being due to air gap and the low emissivity of shocked sample; no temperature was inferred from this data. While the 140 GPa shot may in fact indicate a low emissivity of Fo_{100} at this condition, the result is ambiguous and further low-pressure shots are warranted to resolve this issue as well as to capture the melting transition on the Hugoniot. For the three shots in the range 150–175 GPa where *Lyzenga and Ahrens* [1980] did report temperatures, our interpretation suggests that the emissivity values resulting from their fitting were too low and hence implies that they should have reported lower temperatures for shocked forsterite (see discussion and Figure 11 below).

4.3. $MgSiO_3$ Glass, Enstatite, and Air

[24] The spectral radiance histories for shocked $MgSiO_3$ glass (e.g., Figure 4) and crystal enstatite (e.g., Figure 5) demonstrate air-radiance peaks, due to sample preparation procedures that failed to eliminate the air-gap or produce a sufficiently opaque aluminized surface on the sample. Thus we fit the data to

$$L_\lambda = L_{\lambda b,\mathrm{air}}\epsilon_{\mathrm{air}}e^{-a_s d_s}e^{-a_u d_u} + L_{\lambda b,s}\left(1 - e^{-a_s d_s}\right)e^{-a_u d_u} \quad (9)$$

where $d_s = (U_s - u_p)t$ and $d_u = d_0 - U_s t$. Two extra parameters ($L_{\lambda b,\mathrm{air}}$ and ϵ_{air}) compared to the quartz and olivine cases considered above are required to describe the radiation from the air gap. Because the shock reverberates to a peak pressure within the thin air layer, a_{air} cannot be determined like a_s and a_u. Instead, $L_{\lambda b,\mathrm{air}}$ and ϵ_{air} are coupled as a single parameter ($L_{\lambda,\mathrm{air}}$) in the fitting. The fitted values of a_u reproduce the absorption spectra of the unshocked materials (for enstatite, compare Figure 3 and 7a). The large values of a_s indicate that, at these six wavelengths, the shock-synthesized perovskite from $MgSiO_3$ glass and enstatite may be regarded as blackbody once the thickness of shocked material exceeds ~0.1 mm, i.e., after ~10 ns of shock transit time (Figure 7b).

[25] Figure 8 displays a representative blackbody fitting of $L_{\lambda b,s}$ at six wavelengths to equation (2) for shock temperature of enstatite (shot 340). For comparison we also show a conventional two-parameter gray body fit (at shock exit $L_{\lambda b,s} \sim L_\lambda$, so both fits use the same data points). It is not surprising that the two-parameter gray body fit matches the data better than the one-parameter blackbody fit, but the former yields an unphysical value of $\epsilon = 1.57 \pm 0.44$ and a

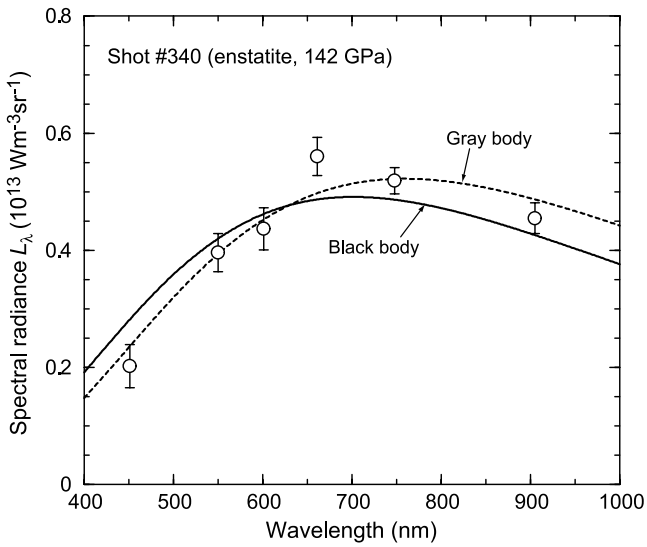

Figure 8. Typical Planck curve fitting of $L_{\lambda b}$ versus λ to equation (2). Note that there is only one parameter T for blackbody fitting as emissivity has already been corrected in $L_{\lambda b}$, even if its absorption were band-like. Apparent radiance L_λ at shock exit is close to $L_{\lambda b}$ as shocked sample is blackbody. Gray body fitting to same data should yield results similar to those from blackbody fitting. A two-parameter gray body fitting is a better fit to the data but yields unphysical $\epsilon = 1.57 \pm 0.44$ and lower $T = 3820 \pm 190$ K compared to $\epsilon = 1$ and $T = 4130 \pm 50$ K, due to the scatter in data. If shocked sample is not a blackbody, L_λ at shock exit is different from $L_{\lambda b}$, thus separate values at shock exit should be used for gray body fitting.

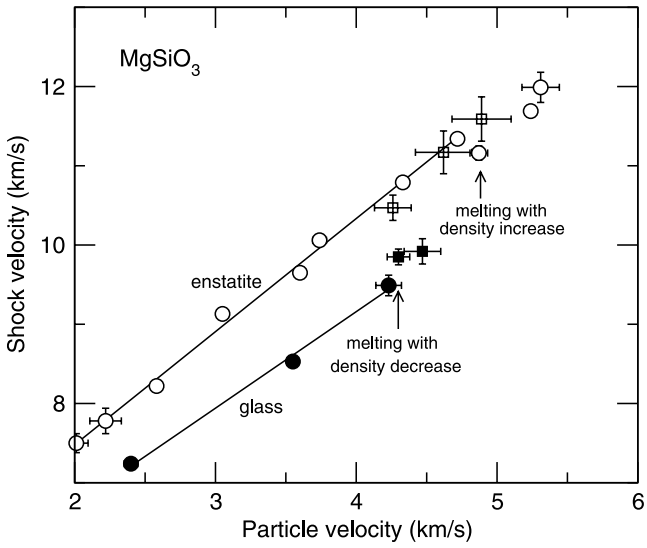

Figure 9. $U_s - u_p$ relations for shocked $MgSiO_3$ glass and enstatite from this work (squares) and *Akins* [2003] (circles). Solid lines are linear fits in Pv regime beyond which Pv melts with positive (on glass Hugoniot) and negative (on enstatite Hugoniot) Clausius-Clapeyron slopes. Note that enstatite data from radiation history (open squares) agree with *Akins* [2003] within experimental uncertainties. In general, the uncertainties in U_s and u_p from radiation history are larger than those from streak-camera diagnostics as employed in *Akins* [2003]. (Some error bars are smaller than the symbol size.)

lower temperature T_H = 3820 ± 190 K (compared to T_H = 4130 ± 50 K for the blackbody fit). This exercise demonstrates that whole-spectrum gray body fitting to data of the spectral resolution and precision available in this kind of experiment can easily yield unphysical or inaccurate results. We are concerned that this kind of trade-off may have affected reported temperature values in previous shock temperature studies (e.g., the forsterite experiments of *Lyzenga and Ahrens* [1980] discussed above) and we recommend the current time-resolved absorption analysis as an alternative.

[26] All three enstatite crystal experiments (340–342) yield fits with estimated uncertainties in T_H that are less than 3%. The values of T_H increase monotonically with shock pressure in the range 142 to 183 GPa (Figure 9). Of the two experiments on enstatite glass, shot 335 yields a result with an uncertainty of ~2%, but the fit for glass shot 336 is based on only two channel recordings and so yields an uncertainty of ~10%. Most likely, T_H increases with P_H in this case, but the difference is not significant. Note that all the uncertainties in T_H reported here are only from the blackbody fitting itself – certainly other possible random or systematic error sources could be contributing as well.

[27] We also deduce values for P_H, U_s and u_p from the radiance histories (Table 2). $U_s - u_p$ pairs for $MgSiO_3$ glass and enstatite were measured from independent shock wave experiments with streak-camera diagnostics [*Akins*, 2003] which are shown as circles in Figure 9 along with our new results (squares). Note that there are apparent slope changes (indicated by arrows) on both glass and enstatite Hugoniots near u_p = 4.23 and 4.72 km/s, respectively. As the density on Hugoniot $\rho_H = \rho_0/(1 - u_p/U_s)$, such slope changes in $U_s - u_p$ indicate phase changes with density increase on glass Hugoniot and decrease on enstatite Hugoniot [*McQueen et al.*, 1970]. In Pv regime, U_s(km/s) = 4.29(0.27) + 1.22(0.08) u_p (glass, ρ_0 = 2.73 g/cm^3; u_p < 4.23 km/s) and U_s(km/s) = 4.63(0.12) + 1.43(0.04)u_p (enstatite, ρ_0 = 3.23 g/cm^3; u_p < 4.72 km/s). Beyond Pv regime, we interpret the phase changes as melting with positive Clausius-Clapeyron slope on $MgSiO_3$ glass Hugoniot and with negative slope on enstatite Hugoniot (also see next section and J. A. Akins et al., Shock induced melting of $MgSiO_3$ perovskite and implications for melts in Earth's lowermost mantle, submitted to *Science*, 2003, hereinafter referred to as Akins et al., submitted manuscript, 2003). Recent studies (M. Murakami et al., Post-perovskite phase transition in $MgSiO_3$, manuscript submitted to *Science*, 2004, and T. Tsuchiya et al., Phase transition in $MgSiO_3$ perovskite in the Earth's lower mantle, manuscript submitted to *Science*, 2004) have documented a solid-solid phase transition in this system, but this does not explain the density decrease on the glass Hugoniot, and the density increase based on the reported equation of state of the post-perovskite phase is inadequate to explain the density increase seen on the enstatite Hugoniot as well.

[28] Our analysis allows the effect of the air gap to be decoupled from the observed spectral radiance. The shock behavior of air is interesting by itself [*Zel'dovich and Raizer*, 2002], with possible ionization, plasma, and chemical reaction effects, but this technique is unlikely to yield useful by-product information on air properties. First, the air radiance depends on driver-sample interface properties (e.g., thickness and coating) that are not necessarily reproducible. Second, the initial pressure in the air gap is unknown, since the sample chamber is pumped to vacuum but the glue holding the sample to the driver may form a partial seal. Third, the shocked thin Al coating could also contribute to the air-radiance. The spectra in the range of 450–900 nm appear band-like rather than gray, yet in the analysis the values of $L_{\lambda b,\mathrm{air}}$ and ϵ_{air} are coupled as $L_{\lambda,\mathrm{air}}$. Nevertheless, as an example, a simple blackbody fitting for shot 340 yields air temperature $T \sim$ 6270 K (peak pressure ~142 GPa).

[29] Note that the emissivities of the shocked silicates are all close to 1 for the wavelengths adopted. This could be due to the combined effects of both temperature and optical roughness (grain size) of the shocked samples [*Siegel and Howell*, 2002]. Possibly, the latter effect is dominant.

5. Geophysical Implications

[30] Our method of obtaining linear absorption coefficients, Hugoniot temperatures, and Hugoniot equation of state data from optical radiance data provides substantial improvement in the precision and accuracy of information on the shock properties of quartz, olivine and forsterite, and its application to the $MgSiO_3$ glass and enstatite study yields new results of geophysical significance. One of the major applications of shock temperature data is the determination of melting behavior at lower-mantle conditions (25 < P < 136 GPa), where static high pressure data on melting are often absent or inconsistent. Here we discuss the implications of our new data and reanalysis of existing data

for possible melting scenarios of Mg-perovskite and its assemblage with MgO at lower mantle conditions based on shock wave and DAC measurements.

5.1. Underlying Logic

[31] The inference of melting curves from Hugoniot temperature information is challenging. It is best to study materials (such as $MgSiO_3$) that melt congruently along a single curve. We do not take into account possible variations in pressure and temperature at melting due to differences between olivine composition and the eutectic point in the high-pressure MgO-$MgSiO_3$ binary. We also neglect the effect of solid solution in the melting Fo_{90}. In the ideal case, equilibrium melting would occur and a sequence of Hugoniot temperature data would be available that capture three regimes: (1) the lower-pressure experiments should be consistent with a calculated Hugoniot for the expected solid assemblage; (2) the intermediate pressure data would achieve equilibrium partial melting states and should follow a plausible equilibrium melting curve with a lower slope dT_H/dP_H due to deposition of some of the increase in internal energy E_H into latent heat of melting, and (3) higher pressure data would again show a steep liquid-phase Hugoniot in $P - T$ space, offset from the extension of the solid Hugoniot by a temperature drop consistent with the entropy of fusion and heat capacity of the material. In a less ideal, but common case, superheating of solids followed by disequilibrium melting occurs such that only two regimes are observed in a sequence of Hugoniot temperatures, separated by a sharp drop in temperature from the highest superheated solid state to a completely molten liquid state Hugoniot point that is on or above the melting curve [*Boness and Brown*, 1993; *Luo and Ahrens*, 2004]. Given the sparse temperature data now available for $MgSiO_3$ and olivine compositions, neither scenario can be resolved with confidence, so the following discussion needs to entertain at least two plausible interpretations of each system.

[32] A well-constrained solid phase Hugoniot will be great help in recognizing melting from Hugoniot temperature data. Here we briefly discuss the calculation of T_H along Hugoniots where solid-solid phase change occurs at high pressures, as is the case here for shock loading low-pressure phases (LPP) such as $MgSiO_3$ glass, enstatite, forsterite and olivine. Suppose that the $U_s - u_p$ relation is known in the high-pressure phase (HPP) regime. An isentrope of HPP centered at standard temperature T_0 and pressure P_0 (STP, denoted as subscript 0) can be constructed (e.g., with third order Birch-Murnaghan EOS given ambient bulk modulus K_{0s} and its pressure derivative K'_{0s}). Temperature along the isentrope is $T_s = T_0 \exp(-\int_{V_0}^{V} \gamma/V \, dV)$ where V is volume and γ Grüneisen parameter. The internal energy increase along an isentrope ΔE_s can be calculated by integrating $P(V)$. At the same volume, the internal energy increase on Hugoniot is $\Delta E_H = 1/2(P_H + P_0)(V_0 - V)$. The pressure difference between the isentrope and Hugoniot at the same volume is due to thermal pressure, assuming a Mie-Grüneisen-type equation of state. Thus T_H can be obtained by solving

$$\Delta E_H = \Delta E_s + E_{\mathrm{tr}} + \int_{T_s}^{T_H} C_v \mathrm{d}T \qquad (10)$$

where E_{tr} is the transformation energy from LPP to HPP at STP and can be estimated from enthalpy of formation. The constant volume heat capacity C_v can be obtained from Debye's model. For simplicity, the Dulong-Petit limit for C_v is adopted. We assume $\gamma = \gamma_0(V/V_0)^q$. For the case $Mg_2SiO_4 \rightarrow MgO + MgSiO_3$, either an isentrope for the mixture is constructed [*Brown et al.*, 1987a] or two separate isentropes are constructed with the assemblage temperature being the sum of T_s weighted by the mass

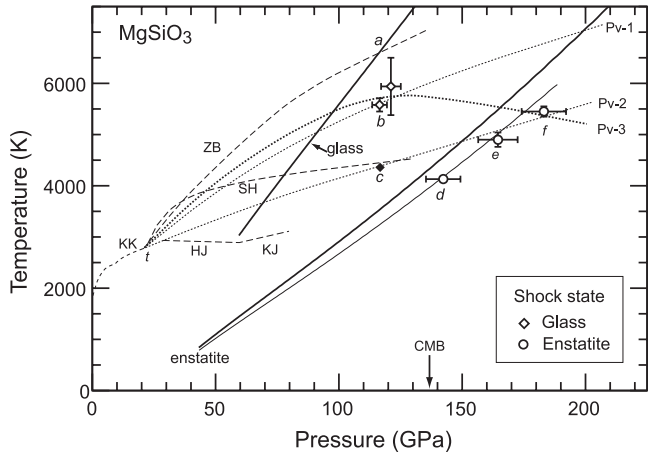

Figure 10. Melting of Mg-perovskite at high pressures: shock wave loading of $MgSiO_3$ glass and enstatite. Dashed curves denote multianvil melting curve by *Kato and Kumazawa* [1985] (KK) and DAC melting curves by *Zerr and Boehler* [1993] (ZB), *Heinz and Jeanloz* [1987] (HJ), *Knittle and Jeanloz* [1989] (KJ) and *Sweeney and Heinz* [1998] (SH). Point *t* is the invariant point where the liquidus intersects the majorite-perovskite reaction and is considered well-known at about 2600 K and 22.5 GPa. Solid curves represent calculated $MgSiO_3$ glass and enstatite Hugoniots assuming the phase in the Hugoniot state is solid perovskite. Two calculated enstatite Hugoniots are shown for $C_v = 3R$ and $3.3R$ (lower solid curve), respectively. Filled diamond (*c*) denotes the melting point calculated if *b* is above melting curve. Dotted curves (Pv-1, 2 and 3) are deduced melting curves (schematic) of perovskite, and Pv-3 is preferred (see text).

Table 3. Parameters for Shock Temperature Calculation

	K_{0s}, GPa	K'_{0s}	γ_0	q	H_0, J/g	$U_s - u_p$
MgO (Pe)[a]	160.3	4.13	1.52	1.0	−14924	
$MgSiO_3$ (Pv)[b]	260.0	3.7	1.5	1.0	−14439	
Pe + Pv[c]	200.0	4	1.5	1.0	−14578	
$MgSiO_3$ (Gl)[d]					−14972	$U_s = 4.29 + 1.22\ u_p$
$MgSiO_3$ (En)[e]					−15395	$U_s = 4.63 + 1.43\ u_p$
Mg_2SiO_4 (Fo)[f]					−15426	$U_s = 3.80 + 1.69\ u_p$

[a] K_0 and K'_0 [*Fei et al.*, 1990]; γ_0 and q [*Akins*, 2003]; H_0 [*Robie et al.*, 1979].

[b] K_0 and K'_0 [*Fiquet et al.*, 2000]; γ_0 and q [*Akins*, 2003]; H_0 [*Saxena et al.*, 1993].

[c] K_0 and K'_0 [*Brown et al.*, 1987b]; γ_0 and q (assumed); H_0: weighted by $\rho_0 = 4.10$ g cm^3.

[d] $U_s - u_p$ [*Akins*, 2003]; H_0 calculated after *Richet and Bottinga* [1986] and *Richet* [1987].

[e] $U_s - u_p$ [*Akins*, 2003]; H_0 [*Berman*, 1988].

[f] $U_s - u_p$ [*Brown et al.*, 1987a]; H_0 [*Robie et al.*, 1979].

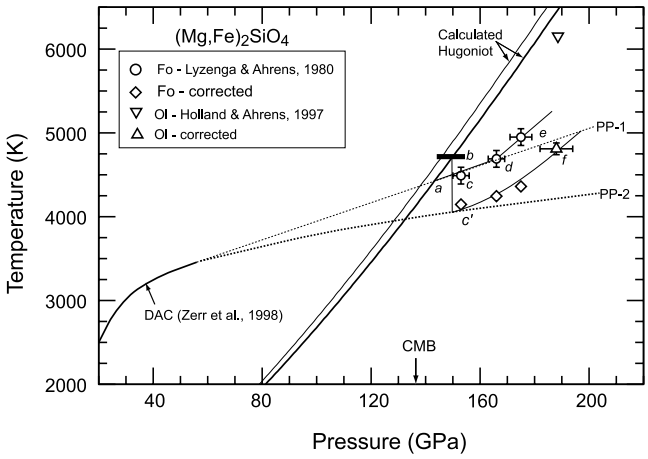

Figure 11. Melting of Mg-perovskite–periclase assemblage: shock wave loading of (Mg, Fe)$_2$SiO$_4$ (Fo and Ol, i.e., forsterite and olivine). Two methods are used to obtain the HPP solid Hugoniot: (1) a single isentrope for Pe-Pv assemblage (upper solid curve) and (2) separate Pe and Pv isentropes (lower solid curve). Horizontal bar centered at *b* is pressure regime where shock melting of (Mg, Fe)$_2$SiO$_4$ occurs [*Brown et al.*, 1987a, 1987b]. Forsterite results (circles) [*Lyzenga and Ahrens*, 1980] are corrected with ϵ = 1 (diamonds). Olivine result (inverted triangle, shot 245 [*Holland and Ahrens*, 1997]; other shots not included) is also shown with our new analysis (triangle). The deviation of measured T_H from calculated Hugoniots suggests shock melting starting near 150 GPa. Two melting curves (PP-1 and 2) are deduced, and PP-2 is preferred for the hypothetical melting of Pe-Pv eutectic.

fractions of the components [*Tan and Ahrens*, 1990]. The parameters used in the solid Hugoniot calculations are listed in Table 3 and calculated shock temperatures are shown in Figures 10–11. Note that all the parameters for calculation are from the literature and may or may not represent the true physical properties.

[33] If a Hugoniot temperature datum is found to be substantially lower than a calculated solid-state Hugoniot, a plausible interpretation is that the Hugoniot state is molten or partially molten and the temperature difference is due to the latent heat of melting. In this case, in order to obtain a constraint on the location of the melting curve $T_m(P)$ it is necessary to distinguish partially molten states (for which $T_H = T_m$) from completely molten states (for which $T_H \geq T_m$). One way to make this distinction is to compare the temperature drop ΔT (relative to extrapolation from the measured or calculated solid-state Hugoniot) to the expected magnitude of cooling required by complete melting at constant pressure and internal energy. The critical temperature drop required for complete melting $\Delta T' \sim T_m \Delta S_m / C_p$ where ΔS_m and C_p are entropy of melting and heat capacity per mole of atoms, respectively. As a reasonable approximation, $C_p \sim 3R$ and $\Delta S_m \sim R\ln 2$ or R where R is the gas constant [*Luo and Ahrens*, 2004]. In principle, $\Delta T < \Delta T'$ indicates partial melting, while for $\Delta T \sim \Delta T'$, it is difficult to distinguish with confidence fully equilibrium melting from a fully molten state already well above the melting curve if a densely sampled data set is not available.

5.2. $MgSiO_3$ Perovskite System

[34] Existing estimates of the high-pressure melting of Mg-perovskite from DAC studies differ. *Zerr and Boehler* [1993] presented a fairly steep melting curve leading to an estimated T_m near the CMB of ~7000 K. On the other hand, the results by Heinz and Jeanloz (1993), *Knittle and Jeanloz* [1989] and *Sweeney and Heinz* [1993] yield lower values of T_m, perhaps 2000–3500 K (Figure 10). Revised data by *Sweeney and Heinz* [1998] agree with *Zerr and Boehler* [1993] at the lower pressures. Below we attempt to place additional constraints on melting of Pv using shock data.

[35] As discussed above, in both the pair of $MgSiO_3$ glass experiments and the set of three enstatite crystal experiments, we see monotonically increasing T_H with P_H in each set, and no break in slope among the three crystal experiments. Hence we do not directly observe melting on either $P - T$ Hugoniot of $MgSiO_3$. Instead, we proceed to gain some inferences from comparison of the measured T_H values to calculated solid perovskite phase Hugoniots (Figure 10). The results are that, if the Hugoniot pressures of the experiments are all correct, then the $MgSiO_3$ glass points (including the well-constrained experiment at point *b*) are $\Delta T \sim 1000$ K below the perovskite Hugoniot centered on glass, whereas the enstatite crystal data are at $\Delta T \sim$ 500–1000 K relative to the perovskite Hugoniot centered on enstatite (the upper one in Figure 10, which assumes C_v = 3R). The magnitude of temperature drop that we expect for complete melting of shocked enstatite is $\Delta T' \geq 1000$ K.

[36] The first interpretation we consider is that all the data are in the solid regime. This would provide no upper bound on the melting curve, and only a very weak lower bound from the maximum plausible amount of superheating [*Luo and Ahrens*, 2003, 2004; *Luo et al.*, 2003a]. The *Zerr and Boehler* [1993] curve is consistent with this, but extrapolations of melting curves (e.g., HJ in Figure 10) indicate melting temperatures below 3000 K at 120 GPa are difficult to satisfy as these require >80% superheating. On the other hand, this interpretation would require either systematic overestimation of our experimental pressures or significant revisions in the parameters used to predict the solid-state HPP Hugoniots, so as to bring the data and the calculation into agreement if the data do indeed represent solid perovskite Hugoniot states. It is also inconsistent with the existence of phase transition (melting) at pressures near *b* and *f* (Figure 10) as indicated by $U_s - u_p$ relations (Figure 9).

[37] The second interpretation is that the well-constrained point *b* on the glass Hugoniot is partially molten and sits on the melting curve, in which case a simple extrapolation of *tb* would yield melting curve Pv-1 which indicates that states $d - f$ are solid. The interpretation that state *b* is partially molten (melt fraction ~0.5–0.8) is consistent with $\Delta T \sim$ 1000 K for point *b*, since a melting point of 5580 K at this pressure would imply $\Delta T' \sim$ 1300–1800 K. This interpretation is consistent with the HPP solid perovskite Hugoniot calculated for glass, but as above would require a revision in the parameters to obtain agreement between the inferred solid states $d - f$ and the HPP Hugoniot centered on enstatite. Improved consistency would result if both solid

Hugoniots were revised downwards by ~500 K. Since the same parameters go into these two calculations (except for H_0 for glass and enstatite, which are well-constrained), both curves would need to be revised. Among all the possibilities of varying the parameters for calculating Hugoniot, the calculated T_H with a revised C_v of ~3.3 R [*Lyzenga et al.*, 1983] would agree with the measurements at $d - f$ and thus support this interpretation. Again, such an interpretation is not consistent with $U_s - u_p$ observations as argued above.

[38] The third interpretation is that b is a fully liquid state above the melting curve. In this case a plausible melting curve Pv-2 could be constructed by assuming $\Delta T \sim \Delta T'$ for experiment b, in which case $T_m = \Delta T C_p/\Delta S_m$ and $C_p/\Delta S_m \sim$ 3/ln2 imply $T_m \sim$ 4300 K (state c). The resulting melting curve through $t - c$ passes close to the enstatite crystal Hugoniot point f, which could then plausibly be either superheated or partially molten. In this case d is most likely in solid state and e is close to the melting curve, i.e., partially molten or solid. The disagreement between solid Hugoniot data and the calculated solid HPP Hugoniot in this case would also be ~500 K. Pv-2 seems plausible as the interpretation of shock temperature is consistent with melting near b and f as suggested by $U_s - u_p$, but its Clausius-Clapeyron slope near f is positive instead of negative as suggested by $U_s - u_p$ relation.

[39] The $U_s - u_p$ relations (Figure 9) suggest that melting with density decrease and increase occurs at pressures near b and f, respectively. Thus a consistent interpretation of shock temperatures and $U_s - u_p$ relations is that the melting curve passes near b with positive Clausius-Clapeyron slope and f with negative slope (Pv-3). Among these three candidate high-pressure melting curves of Pv, Pv-1, 2 and 3, Pv-3 is constrained by both $U_s - u_p$ and temperature data, thus the most plausible; we propose that perovskite melts along Pv-3 with $T_m \sim$ 6000 K and slight density increase [*Akins*, 2003] at the CMB.

5.3. Olivine and Forsterite Systems

[40] Mg_2SiO_4 is expected to disproportionate into MgO (Pe) and $MgSiO_3$ (Pv) at lower mantle conditions [*Presnall*, 1995]. The melting of the Pe-Pv assemblage may be directly relevant, for example to the interpretation of seismic ultralow velocity zones above the core-mantle boundary resolved from travel time and waveform observations [*Garnero and Helmberger*, 1995; *Luo et al.*, 2001, 2002a]. Hugoniot state ($U_s - u_p$) and sound speed measurements on Fo_{100} and Fo_{90} suggest that shock-induced melting occurs at about 145–150 GPa [*Brown et al.*, 1987a, 1987b], which indicates that shock temperature measurements in a pressure range readily achievable with a two-stage light gas gun can be used to explore melting of this assemblage. Eutectic melting of the Pe-Pv assemblage [*Zerr et al.*, 1997] and the solidus of pyrolite [*Zerr et al.*, 1998] have been investigated up to 60 GPa. Shock wave pyrometry has been applied to probe the melting of forsterite [*Lyzenga and Ahrens*, 1980] and of olivine (Fo_{90}, [*Holland and Ahrens*, 1997] at higher pressures, but our study of emissivity and absorption suggests a need to revise the results of these studies. The voltage recordings from the latter study allow us to better define one Hugoniot temperature at ~188 GPa (Figure 11).

[41] Our data analysis has shown that the high-pressure assemblage Pe-Pv of shocked Fo_{100} is essentially blackbody like, whereas *Lyzenga and Ahrens* [1980] obtained gray body fits for Fo_{100} with emissivity in the range of 0.53–0.66. In the following discussion, we still consider the original temperatures of *Lyzenga and Ahrens* [1980] for Fo_{100} as well as corrected values based on $\epsilon = 1$ (Figure 11).

[42] Compared to both methods of calculating the HPP solid Hugoniot, all the revised T_H measurements are appreciably lower than reported earlier, which is consistent with the interpretation of sound speed results (as well as $U_s - u_p$) showing that all these points should be molten (Figure 11). We consider two scenarios of melting: equilibrium and non-equilibrium (with superheating). If we adopt the original temperatures of *Lyzenga and Ahrens* [1980], points $c - e$, then melting curve PP-1 is consistent with states c and d representing partial melting and e indicating complete melting. Thus acd is the segment of the Hugoniot representing equilibrium melting of the Pe-Pv assemblage. But if the solidus depression due to fayalite component is small, then state f for Fo_{90} seems inconsistent with such an interpretation. States e and f cannot both represent fully molten states (even if the melting curve has a negative slope in this region like Pv) as in this case the temperature drop from e to f cannot represent consumption of latent heat. On the other hand, if the corrected temperatures for Fo_{100} (diamonds) are adopted, we can construct a superheating-melting curve $abc'f$; i.e., with increasing Hugoniot pressure, the Pe-Pv assemblage is superheated to ~150 GPa, then melts and achieves temperature close to the melting curve (c'), followed by liquid Hugoniot $c'f$. We thus approximate the melting curve as PP-2. The melting temperature of the Pe-Pv assemblage at olivine bulk composition at the pressure of the CMB in these two scenarios is estimated as ~4000 K and 4400 K, respectively. PP-2 is favored because it applies a consistent methodology to emissivity determination in all the data and better explains the radiation history of the *Lyzenga and Ahrens* [1980] experiments.

[43] More shock wave data would help with resolving the ambiguities in these interpretations, which remain to be investigated in the future. On the basis of the arguments above, we propose that the melting temperatures at the CMB are about 6000 ± 500 K for Mg-perovskite, and 4000 ± 300 K for olivine composition undergoing eutectic melting as a Pe-Pv assemblage (Uncertainties are estimated). These values are consistent with the prediction by *Boehler* [2000] that liquids in equilibrium with lower mantle minerals are very rich in MgO at CMB pressures. Once experiments firmly establish these melting points, interpretation of possible partial melting zones in ULVZs at the base of the mantle will depend on constraining the lower mantle adiabat, the temperature contrast across the core-mantle thermal boundary layer, the melting temperature of core alloys, and the role of chemical heterogeneities and minor components in the D″ layer. Of particular interest is that if the lower mantle adiabat allows melting, Pv melt may be denser than its solid counterpart. This suggests that locally formed dense Pv melt (e.g., at ULVZ's) is more resistant to upwelling

driving force and thus more stable (Akins et al., submitted manuscript, 2003).

6. Conclusion

[44] Shock wave optical pyrometry experiments on $MgSiO_3$ glass, enstatite, olivine and quartz yield time- and wavelength-resolved spectral radiances. The shock travel time inferred from digital oscilloscope recordings of optical radiation is consistent with previous Hugoniot equations of state measured with streak camera or other diagnostics. At each wavelength, the optical absorption coefficients and blackbody spectral radiances of the shocked and unshocked samples were obtained by fitting to the radiation history. The linear absorption coefficients indicate blackbody radiation of shock-synthesized high-pressure phases (once thickness of the shocked layer exceeds 1 mm) in the wavelength range investigated. However, unshocked crystalline enstatite and Fe-bearing olivine are shown to have absorption bands in their spectra that complicate effective gray body fitting of radiation emerging from partly shielded shock fronts. We suggest downwards revisions in the shock temperatures for olivine previously published by *Lyzenga and Ahrens* [1980] and *Holland and Ahrens* [1997]. Temperatures of shock-synthesized Mg-perovskite and its assemblage with periclase provide constraints on their high-pressure melting curves. It is suggested that Mg-perovskite melts with density increase at the CMB pressure, and that the melting temperatures at the CMB are about 6000 ± 500 K for Mg-perovskite, and 4000 ± 300 K for the Mg-perovskite-periclase assemblage.

[45] **Acknowledgments.** This work was supported by U.S. National Science Foundation Grant No. EAR-0207934 (TJA and PDA). SNL is sponsored by a Director's Post-doctoral Fellowship at Los Alamos National Laboratory (P-24 and EES-11). P. Gelle, M. Long and C. McCaughey supplied invaluable technical support. G. R. Rossman and E. Arrendondo kindly helped with optical spectroscopy measurements. C. Francis and S. Mackwell supplied the high-quality Sri Lanka enstatite crystals. We also benefited from discussions with X. L. Huang, S. D. Ni and D. C. Swift. The constructive suggestions by D. Heinz and I. Jackson are highly appreciated. Contribution No. 8951, Division of Geological and Planetary Sciences, California Institute of Technology.

References

Ahrens, T. J., D. L. Anderson, and A. E. Ringwood (1969), Equations of state and crystal structures of high-pressure phases of shocked silicates and oxides, *Rev. Geophys.*, *7*, 667–707.

Akins, J. A. (2003), Dynamic compression of minerals in MgO-FeO-SiO_2 system, Ph.D. thesis, Calif. Inst. of Technol., Pasadena, Calif.

Akins, J. A., S.-N. Luo, P. D. Asimow, and T. J. Ahrens (2003), Shock induced melting of $MgSiO_3$ perovskite and implications for melts in Earth's lowermost mantle, submitted to *Science*.

Berman, R. G. (1988), Internally-consistent thermodynamic data for minerals in the system Na_2O-K_2O-CaO-MgO-FeO-Fe_2O_3-Al_2O_3-SiO_2-TiO_2-H_2O-CO_2, *J. Petrol.*, *29*, 445–522.

Boehler, R. (2000), High-pressure experiments and the phase diagram of lower mantle and core materials, *Rev. Geophys.*, *38*, 221–245.

Boness, D. A., and J. M. Brown (1993), Bulk superheating of solid KBr and CsBr with shock-waves, *Phys. Rev. Lett.*, *71*, 2931–2934.

Boslough, M. B. (1985), A model for time dependence in shock-induced thermal radiation of light, *J. Appl. Phys.*, *58*, 3394–3399.

Boslough, M. B., and T. J. Ahrens (1989), A sensitive time-resolved radiation pyrometer for shock-temperature measurements above 1500 K, *Rev. Sci. Instrum.*, *60*, 3711–3716.

Brown, J. B., M. D. Furnish, and R. G. McQueen (1987a), Sound speed measurements of (Mg, Fe)$_2SiO_4$, in *Shock Waves in Condensed Matter-1987*, edited by S. C. Schmidt and N. C. Holmes, pp. 119–122, Elsevier Sci., New York.

Brown, J. B., M. D. Furnish, and R. G. McQueen (1987b), Thermodynamics for (Mg, Fe)$_2SiO_4$ from the Hugoniot, in *High-Pressure Research in Mineral Physics*, edited by M. H. Manghnani and Y. Syono, pp. 373–384, AGU, Washington, D. C.

Burns, R. G. (1993), *Mineralogical Applications of Crystal Field Theory*, 2nd ed., Cambridge Univ. Press, New York.

Fei, Y., S. K. Saxena, and A. Navrotsky (1990), Internally consistent thermodynamic data and equilibrium phase relations for compounds in the system MgO-SiO_2 at high pressure and high temperature, *J. Geophys. Res.*, *95*, 6915–6928.

Fiquet, G., A. Dewaele, D. Andrault, M. Kunz, and T. Le Bihan (2000), Thermoelastic properties and crystal structure of $MgSiO_3$ perovskite at the lower mantle pressure and temperature conditions, *Geophys. Res. Lett.*, *27*, 21–24.

Fowles, G. R. (1989), *Introduction to Modern Optics*, pp. 203–217, Dover, Mineola, N. Y.

Garnero, E. J., and D. V. Helmberger (1995), A very slow basal layer underlying large-scale low-velocity anomalies in the lower most mantle beneath the Pacific – evidence from core phases, *Phys. Earth Planet. Inter.*, *91*, 161–176.

Grand, S., R. van der Hilst, and S. Widiyantoro (1997), Global images of the Earth's interior, *GSA Today*, *7*, 1–7.

Heinz, D. L., and R. Jeanloz (1987), Measurement of the melting curve of $Mg_{0.9}Fe_{0.1}SiO_3$ at lower mantle conditions and its geophysical implications, *J. Geophys. Res.*, *92*, 1437–1444.

Holland, K. G. (1997), Phase diagram and transport properties of geophysical materials under shock loading, Ph.D. thesis, Calif. Inst. of Technol., Pasadena, Calif.

Holland, K. G., and T. J. Ahrens (1997), Melting of (Mg, Fe)$_2SiO_4$ at the core-mantle boundary of the Earth, *Science*, *275*, 1623–1625.

Jackson, I., and T. J. Ahrens (1979), Shock wave compression of single-crystal forsterite, *J. Geophys. Res.*, *84*, 3039–3048.

Jackson, J. D. (1975), *Classical Electrodynamics*, John Wiley, Hoboken, N. J.

Kato, T., and M. Kumazawa (1985), Garnet phase of $MgSiO_3$ filling the pyroxene ilmenite gap at very high-temperature, *Nature*, *316*, 803–805.

Knittle, E., and R. Jeanloz (1989), Melting curve of (Mg, Fe)SiO_3 perovskite to 96 GPa: Evidence for a structural transition in lower mantle melts, *Geophys. Res. Lett.*, *16*, 421–424.

Kormer, S. B. (1965), Optical study of the characteristics of shock-compressed dielectrics, *Sov. Phys. Usp., Engl. Transl.*, *21*, 689–700.

Luo, S.-N., and T. J. Ahrens (2003), Superheating systematics of crystalline solids, *Appl. Phys. Lett.*, *82*, 1836–1839.

Luo, S.-N., and T. J. Ahrens (2004), Shock-induced superheating and melting curves of geophysically important minerals, *Phys. Earth Planet. Inter.*, in press.

Luo, S.-N., S. D. Ni, and D. V. Helmberger (2001), Evidence for a sharp lateral variation of velocity at the core-mantle boundary from multipathed PKPab, *Earth Planet. Sci. Lett.*, *189*, 155–164.

Luo, S.-N., S. D. Ni, and D. V. Helmberger (2002a), Relationship of D″ structure with the velocity variations near the inner-core boundary, *Geophys. Res. Lett.*, *29*(11), 1527, doi:10.1029/2001GL013907.

Luo, S.-N., J. L. Mosenfelder, P. D. Asimow, and T. J. Ahrens (2002b), Direct shock wave loading of stishovite to 235 GPa: Implications for perovskite stability relative to an oxide assemblage at lower mantle conditions, *Geophys. Res. Lett.*, *29*(14), 1691, doi:10.1029/2002GL015627.

Luo, S.-N., T. J. Ahrens, T. Çağin, A. Strachan, W. A. Goddard III, and D. C. Swift (2003a), Maximum superheating and undercooling: Systematics, molecular dynamics simulations and dynamic experiments, *Phys. Rev. B.*, *68*, 134–206.

Luo, S.-N., T. J. Ahrens, and P. D. Asimow (2003b), Polymorphism, superheating and amorphization of silica upon shock wave loading and release, *J. Geophys. Res.*, *108*(B9), 2421, doi:10.1029/2002JB002317.

Luo, S.-N., D. C. Swift, T. Tierney, K. Xia, O. Tschauner, and P. D. Asimow (2004), Time-resolved X-ray diffraction investigation of superheating-melting behavior of crystals under ultrafast heating, in *Shock Compression of Condensed Matter-2003*, edited by M. D. Furnish, Am. Inst. of Phys., College Park, Md., in press.

Lyzenga, G. A. (1980), Shock temperatures of materials: Experiments and applications to the high pressure equation of state, Ph.D. thesis, Calif. Inst. of Technol., Pasadena, Calif.

Lyzenga, G. A., and T. J. Ahrens (1980), Shock temperature measurements in Mg_2SiO_4 and SiO_2 at high pressures, *Geophys. Res. Lett.*, *7*, 141–144.

Lyzenga, G. A., T. J. Ahrens, and A. C. Mitchell (1983), Shock temperatures of SiO_2 and their geophysical implications, *J. Geophys. Res.*, *88*, 2431–2444.

McQueen, R. G., S. P. Marsh, J. W. Taylor, J. N. Fritz, and W. J. Carter (1970), The equation of state of solids from shock wave studies, in *High Velocity Impact Phenomena*, edited by R. Kinslow, pp. 294–417, Academic, San Diego, Calif.

Mitchell, A. C., and W. J. Nellis (1981), Shock compression of aluminum, copper, and tantalum, *J. Appl. Phys.*, *52*, 3363–3374.

Ni, S. D., E. Tan, M. Gurnis, and D. V. Helmberger (2002), Sharp sides to the Africa superplume, *Science*, *296*, 1850–1852.

Presnall, D. C. (1995), Phase-diagrams of Earth-forming minerals, in *Mineral Physics and Crystallography, A Handbook of Physical Constants*, vol. 2, edited by T. J. Ahren, pp. 248–268, AGU, Washington, D. C.

Richet, P. (1987), Heat-capacity of silicate-glasses, *Chem. Geol.*, *62*, 111–124.

Richet, P., and Y. Bottinga (1986), Thermochemical properties of silicate glasses and liquids: A review, *Rev. Geophys.*, *24*, 1–25.

Robie, R. A., S. H. Bruce, and J. R. Fisher (1979), *Thermodynamic Properties of Minerals and Related Substances at 298.15 K and 1 Bar (10^5 Pascals) Pressure and at Higher Temperatures*, U.S. Gov. Print. Off., Washington, D. C.

Saxena, S. K., N. Chatterjee, Y. Fei, and G. Shen (1993), *Thermodynamic Data on Oxides and Silicates*, Springer-Verlag, New York.

Shen, G. Y., and P. Lazor (1995), Measurement of melting temperatures of some minerals under lower mantle pressures, *J. Geophys. Res.*, *100*, 17,699–17,713.

Siegel, R., and J. R. Howell (2002), *Thermal Radiation Transfer*, 4th ed., Taylor and Francis, London.

Sweeney, J. S., and D. L. Heinz (1993), Melting of iron-magnesium-silicate perovskite, *Geophys. Res. Lett.*, *20*, 855–858.

Sweeney, J. S., and D. L. Heinz (1998), Laser-heating through a diamond-anvil cell: Melting at high pressures, in *Properties of Earth and Planetary Materials at High Pressure and Temperature*, edited by M. H. Manghnani and T. Yagi, pp. 197–213, AGU, Washington, D. C.

Swift, D. C., G. J. Ackland, A. Hauer, and G. A. Kyrala (2001), First-principles equations of state for simulations of shock waves in solids, *Phys. Rev. B*, *64*, 214107.

Tan, H., and T. J. Ahrens (1990), Shock-induced polymorphic transition in quartz, carbon, and boron nitride, *J. Appl. Phys.*, *67*, 217–224.

Zel'dovich, Ya. B., and Yu. P. Raizer (2002), *Physics of Shock Waves and High-temperature Hydrodynamic Phenomena*, Dover, Mineola, N. Y.

Zerr, A., and R. Boehler (1993), Melting of (Mg, Fe)SiO_3-Perovskite to 625 kilobars: Indication of a high melting temperature in the lower mantle, *Science*, *262*, 553–555.

Zerr, A., G. Sergiou, and R. Boehler (1997), Melting of $CaSiO_3$ perovskite to 430 kbar and first in-situ measurements of lower mantle eutectic temperatures, *Geophys. Res. Lett.*, *24*, 909–912.

Zerr, A., A. Diegeler, and R. Boehler (1998), Solidus of Earth's deep mantle, *Science*, *281*, 243–246.

T. J. Ahrens, J. A. Akins, and P. D. Asimow, Division of Geological and Planetary Sciences, California Institute of Technology, Pasadena, CA 91125, USA.

S.-N. Luo, Plasma Physics (P-24), MS E526, Los Alamos National Laboratory, Los Alamos, NM 87545, USA. (sluo@lanl.gov)